Supporting Information

A Design Concept for Halogen-free Mg^{2+}/Li$^+$-Dual Salt-Containing Gel-Polymer-Electrolytes for Rechargeable Magnesium Batteries

Peiwen Wang[1], Janina Trück[1,3], Joachim Häcker[4], Anja Schlosser[5], Kathrin Küster[6], Ulrich Starke[6], Leonie Reinders[2] and Michael R. Buchmeiser[1,2]*

[1]Institute of Polymer Chemistry, University of Stuttgart, 70569, Stuttgart, Germany

[2] German Institutes of Textile and Fiber Research (DITF), 73770 Denkendorf, Germany

[3]Daimler AG, 70327 Stuttgart, Germany

[4]Institute of Engineering Thermodynamics, German Aerospace Center, 70569 Stuttgart, Germany

[5]Customcells Holding GmbH, 25524 Itzehoe, Germany

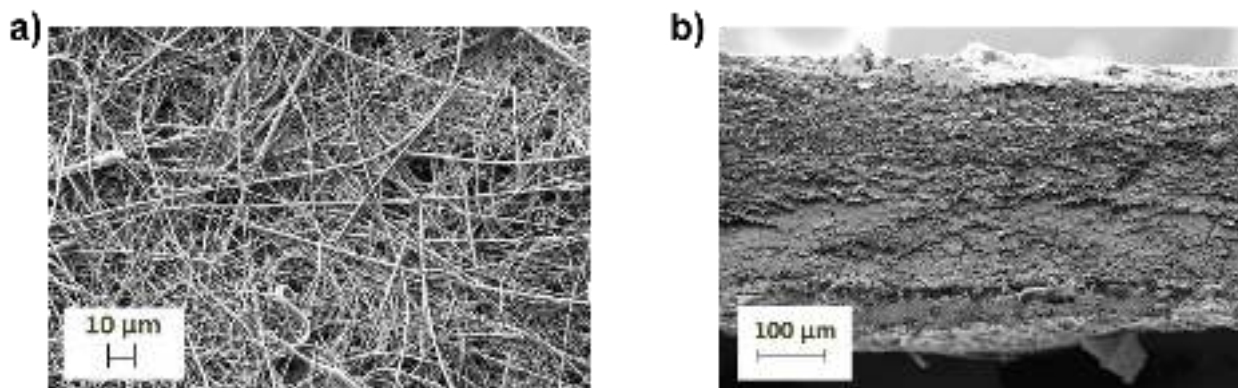[6]Max Planck Institute for Solid State Research, 70569 Stuttgart, Germany

Corresponding Author

*Email: michael.buchmeiser@ipoc.uni-stuttgart.de*

# Content

Section 1. Supporting Figures

Figure S1. SEM images of **a)** the surface of a pristine glass fiber separator; **b)** a cross-section of the MLT-GPE.

The comparison between a pristine glass fiber separator and an magnesium, lithium, TiO_2-gel polymer electrolyte (MLT-GPE) (Figure S1a), together with the SEM image of the cross-section of the MLT-GPE, confirms that the pores in the glass fiber separator are infiltrated by the MLT-GPE after the *in-situ* cross-linking reaction.
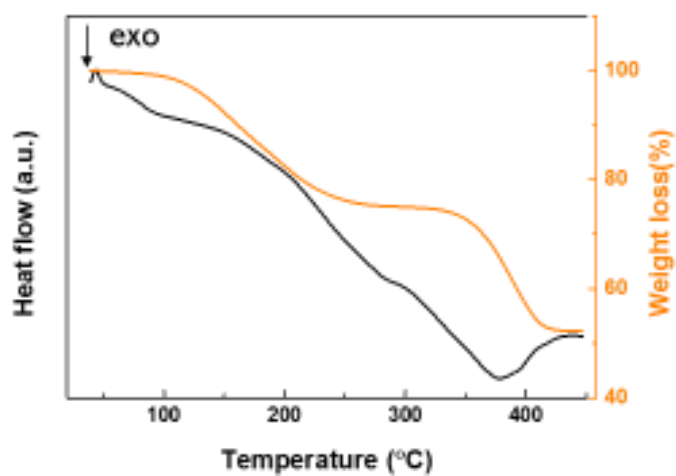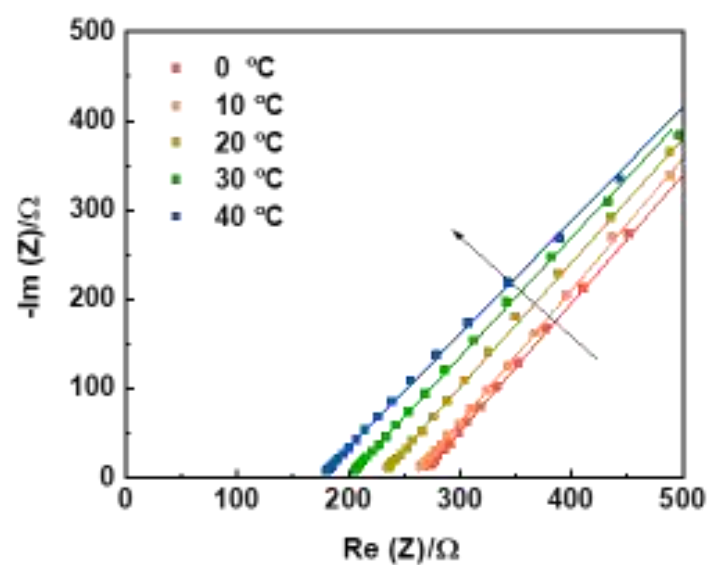
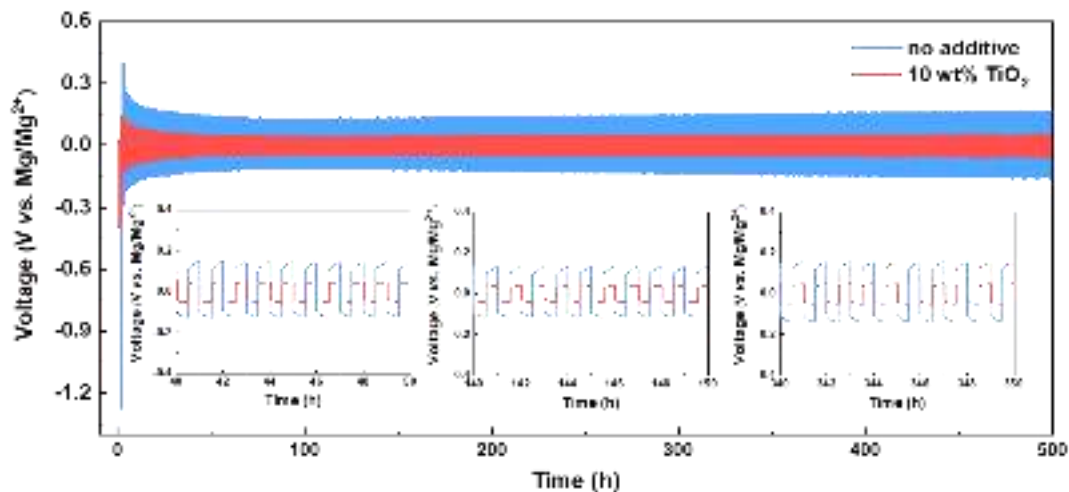**Figure S2.** TGA-DSC analysis of the MLT-GPE.

Figure S2 shows the TGA-DSC results of the MLT-GPE. The crosslinked MLT-GPE shows a higher melting temperature (380 °C) than the reactants (PTHF, 28 °C).[1]
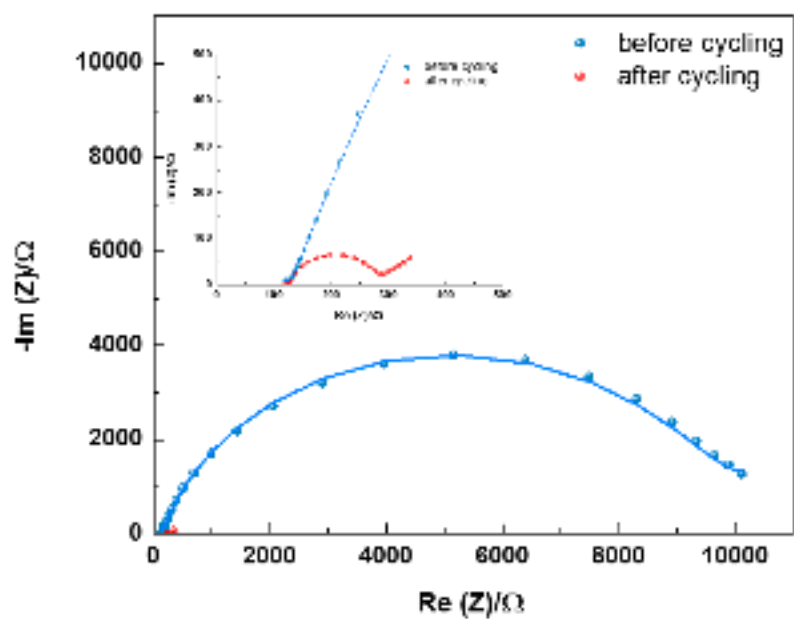
**Figure S3.** Nyquist plots of the Mg|| MLT-GPE || Mg cell with an before and after cycling.

**Figure S4.** Nyquist plots of the SS||GPE||SS cell without TiO_2 at different temperatures.

Figure S5. Long-term galvanostatic cycling of symmetric Mg||Mg cells at 0.1 mA cm^{-2} with various amounts of TiO$_2$ as additive. Blue: 0.1 M Mg[BH$_4$]$_2$ and 1.5 M Li[BH$_4$] in diglyme + PTHF/THF; red: 0.1 M Mg[BH$_4$]$_2$ and 1.5 M Li[BH$_4$] and 10 wt% TiO$_2$ in diglyme + PTHF/THF (MLT-GPE).

The overpotentials of the symmetric cells using the GPE with/without TiO$_2$ nanoparticles were compared at 0.1 mA cm^{-2} (Figure S5). The GPE without TiO$_2$ nanoparticles shows nearly twice the overpotential than the one with TiO$_2$ nanoparticles, indicating the comprehensive improvement of the conductive behavior by the introduction of TiO$_2$ nanoparticles.
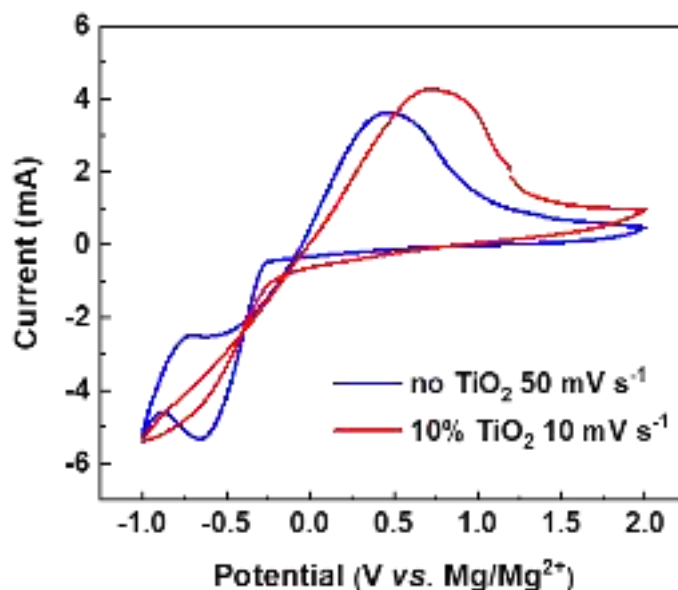
Figure S6. Cyclic voltammetry (CV) of Mg-stainless steel cells using gel polymer electrolytes with and without TiO_2. Red: 0.1 M $Mg[BH_4]_2$ and 1.5 M $Li[BH_4]$ and 10 wt% TiO_2 in diglyme + PTHF/THF (MLT-GPE); scan rate: 10 mV·s^{-1}; blue: 0.1 M $Mg[BH_4]_2$ and 1.5 M $Li[BH_4]$ in diglyme + PTHF/THF; scan rate: 50 mV·s^{-1}.

A Mg||SS cell without TiO_2 nanoparticles and a Mg||SS cell with the MLT-GPE was subjected to cyclic voltammetry applying a scan rate of 50 and 10 mV s^{-1}, respectively (Figure S6). The Mg||SS cell with the MLT-GPE shows higher current density even at a slower scan rate, demonstrating the improvements of the cell performance by the TiO_2 nanoparticles.
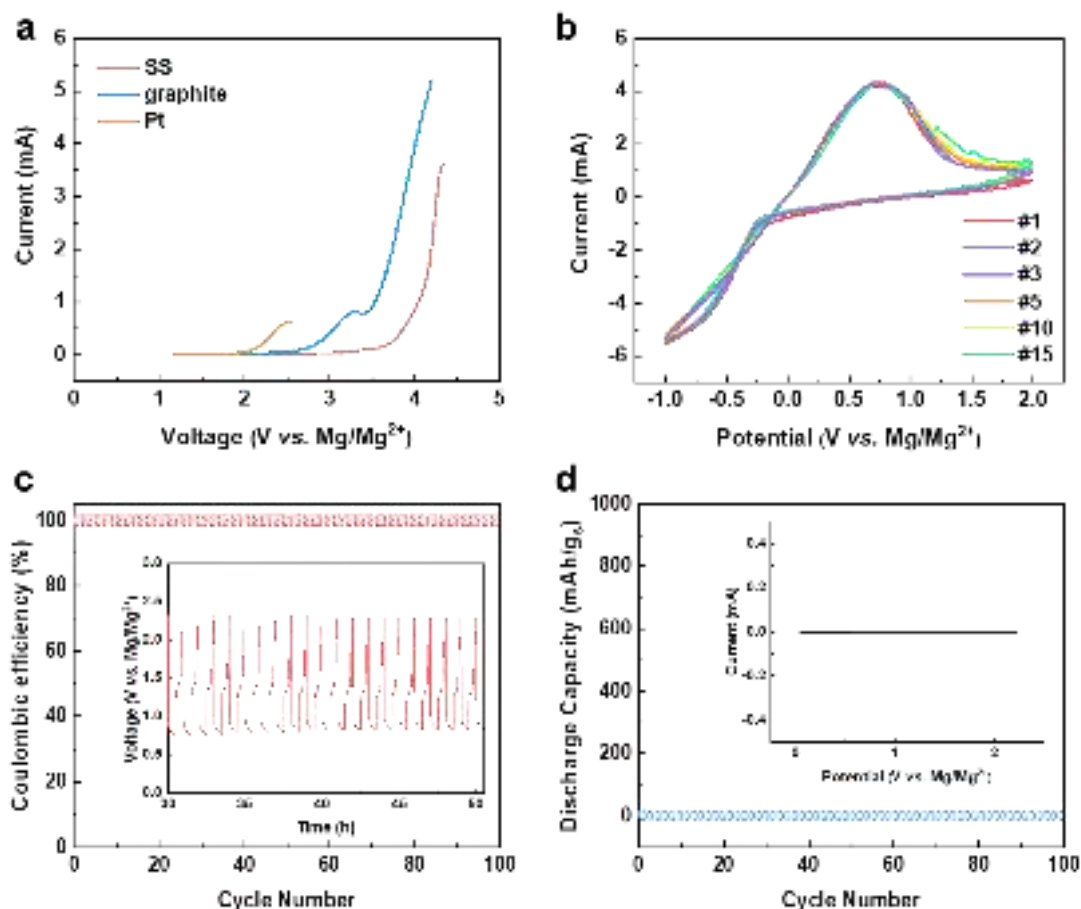
Figure S7. Electrochemical measurements with MLT-GPE as electrolyte: **a)** linear sweep voltammetry (LSV) with Mg foil as counter electrode, stainless steel foil/graphite foil/platinum foil as working electrode; **b)** cyclic voltammetry (CV) of Mg-stainless steel cell; scan rate: 10 mV·s^{-1}; **c)** coulombic efficiency measurements using a Mg-stainless steel cell; inset: corresponding potential curve; **d)** discharge capacity and CV (inset) of Mg-stainless steel cell, measured in a voltage window of 0.05 V to 2.3 V.

Figure S7a shows the LSV results of the MLT-GPE against three different current collectors (Pt, graphite, stainless steel). Common current collectors such as Al or carbon-coated Al foil were not tested due to the known poor corrosion resistance.[2] According to Figure S7a, the highest voltages of these current collectors (Pt, graphite and stainless steel), at which they are still stable towards oxidation, are 2 V, 2.6 V and 3.6 V, respectively. The solvents inside the gel[3] can be made accountable for the finding that

the Pt current collector does not show the best corrosion resistance. Stainless steel foil was therefore used as current collector due to its low costs and good corrosion resistance.

Figure S7d shows the galvanostatic cycling and CV of a Mg||SS cell to examine whether the stainless steel current collector was inert and the MLT-GPE contributed to the capacity in the voltage window (0.05 V to 2.3 V). Negligible discharge capacity (<1 mAh/g) was detected in the applied voltage window. Also, no signals in CV were detected in this voltage range. Therefore, in the following electrochemical cycling tests, the voltage window was set from 0.05 V to 2.3 V.
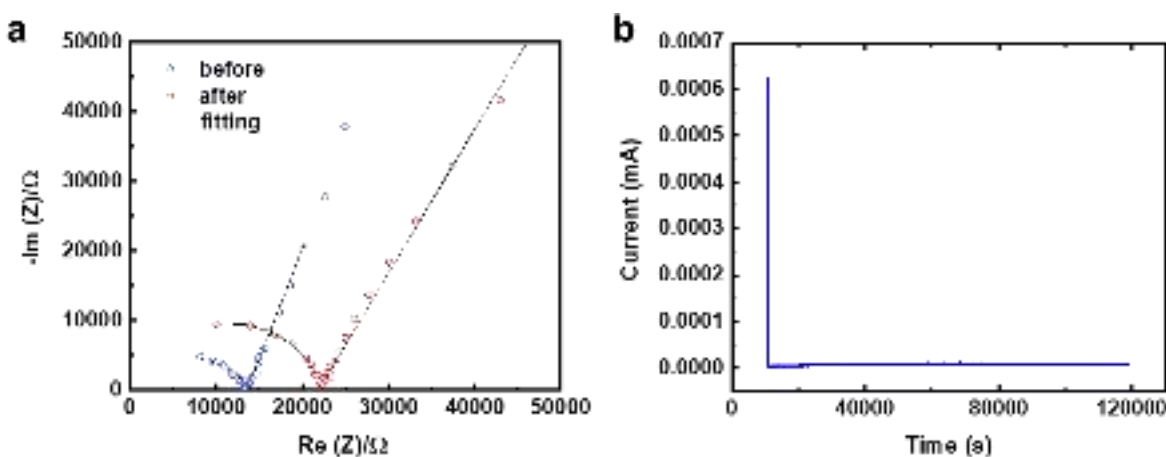

Figure S8. a) Nyquist plots of the Mg^{2+} electrolyte. The red curve shows the impedance spectrum after polarization. The blue curve shows the impedance spectrum before polarization at steady state. The black curves represent the fitting; **b)** chronoamperogram of a Mg^{2+} electrolyte with an applied voltage of 10 mV.

In order to exclude the influence of Li^+, the transfer number of Mg^{2+} was measured based on the Bruce and Vincent method (Eq.S1) using a pure Mg^{2+} electrolyte, 0.1 M $Mg[BH_4]_2$, 10 wt% TiO_2 in diglyme, with the addition of PTHF/THF (Figure S8). A small constant potential (10 mV) was applied to the electrolyte between two magnesium electrodes, leading to a decrease of the initial current value (0.623 mA) until steady state (8.9 µA) after 2000 minutes (Figure S8b). Since the anions are not involved in the redox reaction, the anion current vanishes after reaching the steady state and the total current is only caused by the Mg^{2+} cations. The contact resistance was measured before and after polarization. Figure S8a shows the chronoamperometric and impedance

measurement using the Mg^{2+} electrolyte. The fitted resistance values are listed in Table S3. The transfer number of the Mg^{2+} was further determined by Eq. S1:

$$t_{Mg^{2+}} = \frac{I_{SS}\left(\Delta V - I_0 R_{P,0}\right)}{I_0\left(\Delta V - I_{SS} R_{P,SS}\right)} = \frac{8.938\ \mu A \times (10\ mV - 623\ \mu A \times 4.4\ k\Omega)}{623\ \mu A \times (10\ mV - 8.938\ \mu A \times 10.34\ k\Omega)} = 0.5 \tag{S1}$$
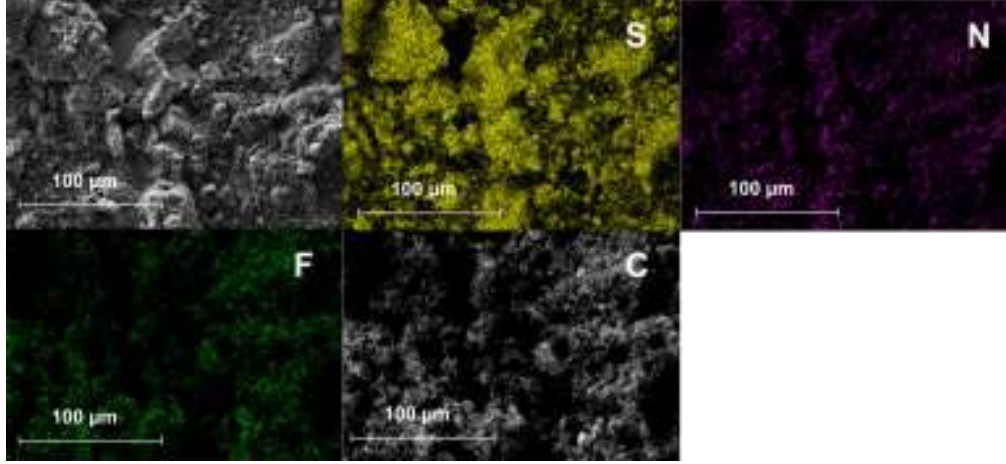

Figure S9. SEM image and elemental mapping of the SPAN cathode.

The elemental mapping of the SPAN cathode shows good homogeneity (Figure S9). Signals for S and N stem from the SPAN structure. Signals for F stem from the binder (PVDF). The C signals stem from conducting super carbon 65, PVDF and SPAN.
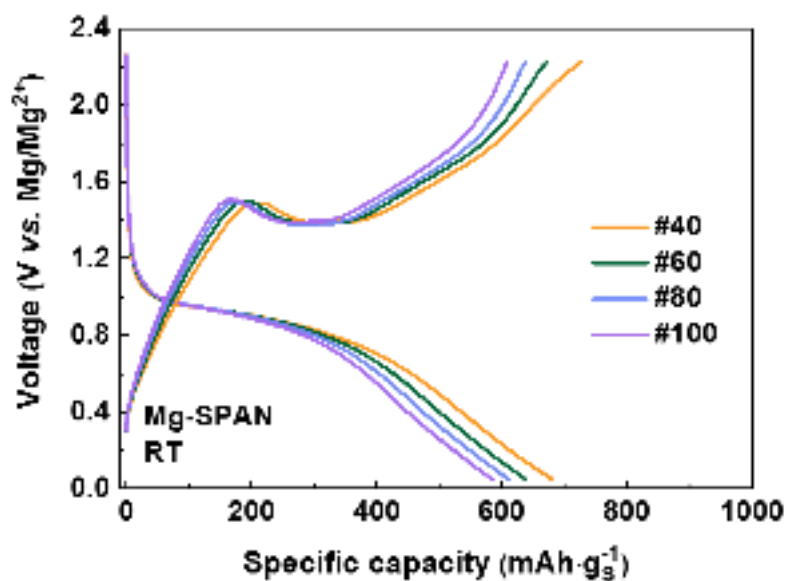
Figure S10. Voltage curves of the Mg||MLT-GPE||SPAN cell shown in Figure 3a. The voltage curves show the characteristics SPAN features. In the discharge curve, a plateau at around 1 V represents the formation of short chain polysulfides MgS_x (x<4).
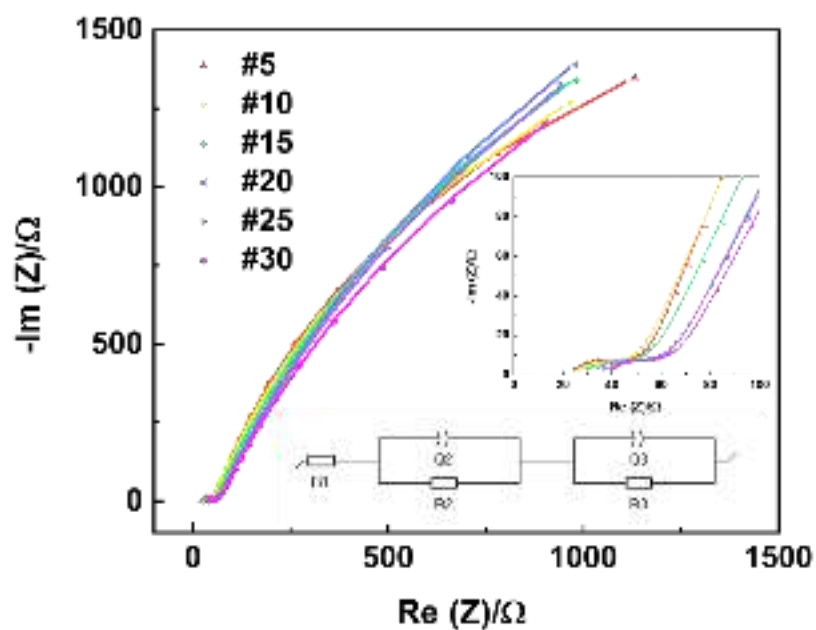
Figure S11. Nyquist plot of a Mg-SPAN cell after 5, 10, 15, 20, 25 and 30 cycles. Dots: experimental data; line: fitted data (by the inset equivalent circuit model); where R_1 is the bulk resistance, R_2 represents the resistance of the solid electrolyte interphase (SEI) layer on the Mg anode; R_3 is the charge transfer resistance between the active material (SPAN) and the electrolyte.[4]
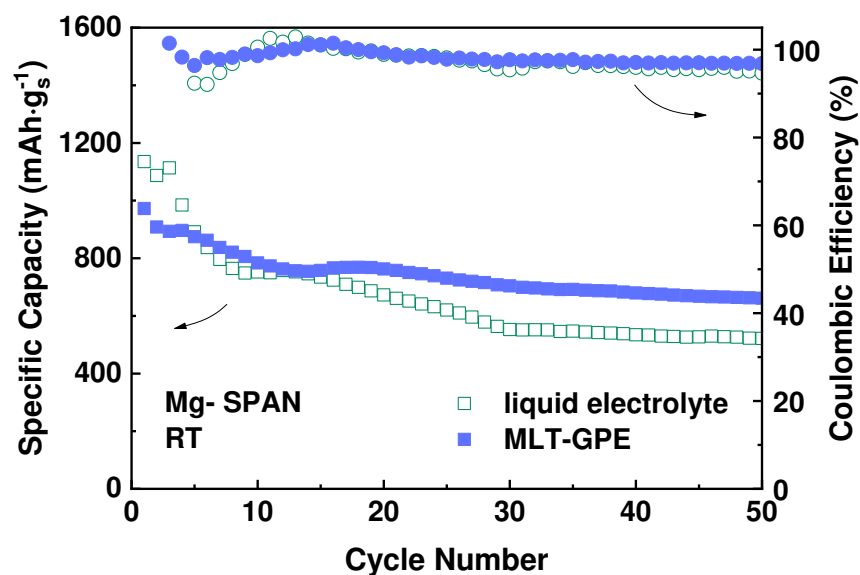
Figure S12. Performance comparison of Mg-SPAN cells cycled with the liquid electrolyte (green, 0.1 M Mg[BH$_4$]$_2$, 1.5 M Li[BH$_4$], 10 wt% TiO$_2$ in diglyme) and the MLT-GPE (blue) at 0.2 C at room temperature.

The Mg||MLT-GPE||SPAN cell shows better capacity retention than the Mg||liquid electrolyte||SPAN cell, indicating successful suppression of the polysulfide shuttle in the MLT-GPE. Nonetheless, the Mg||liquid electrolyte||SPAN cell still shows acceptable cycle performance compared to other reported systems (Table S4), attributable to an effective retaining of sulfur by covalently bound S in the SPAN structure.
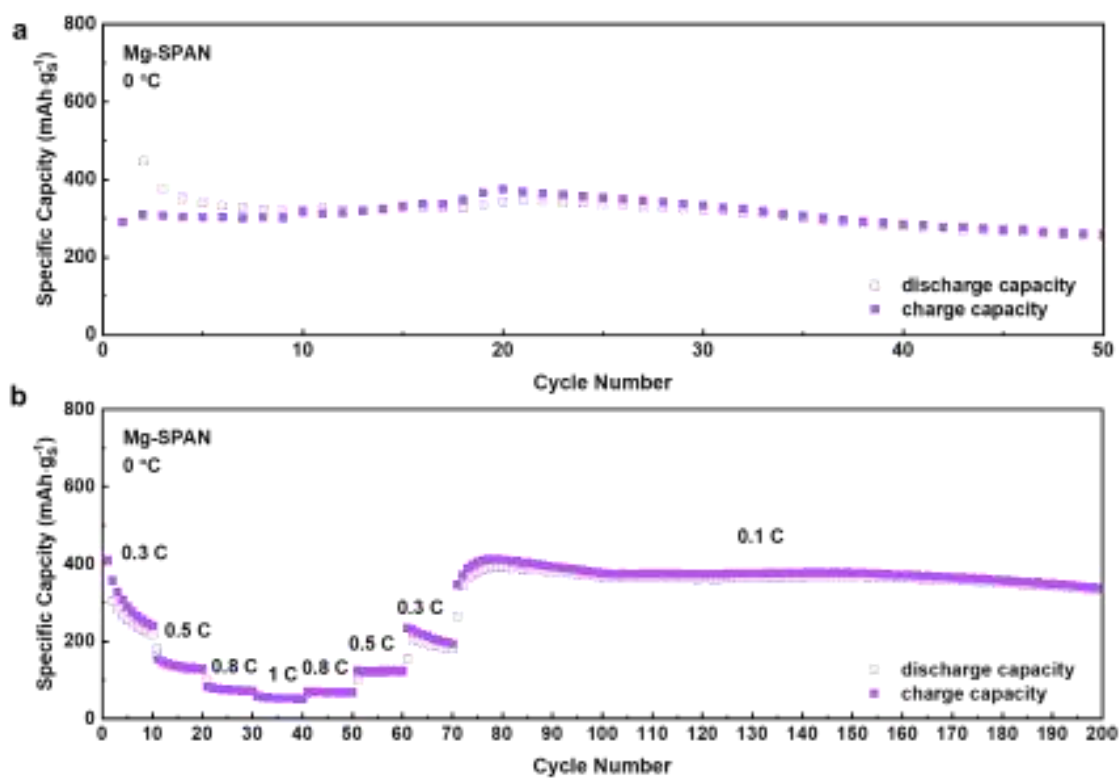
Figure S13. a) Long-term cycling data at 0.2 C and 0 ℃; **b)** rate capability results of the Mg||MLT-GPE||SPAN cell cycled at 0 ℃.
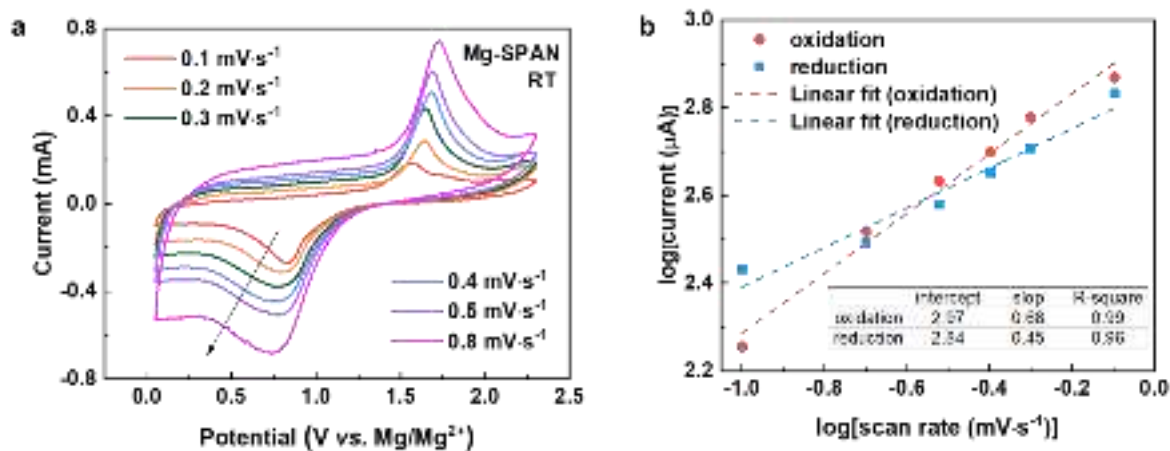
Figure S14. a) Cyclic voltammetry (CV) curves of the Mg||MLT-GPE||SPAN cell at different scan rates (0.1 mV·s^{-1} to 0.8 mV·s^{-1}); **b)** logarithm of the anodic and cathodic peak currents versus the logarithm of the scan rate.
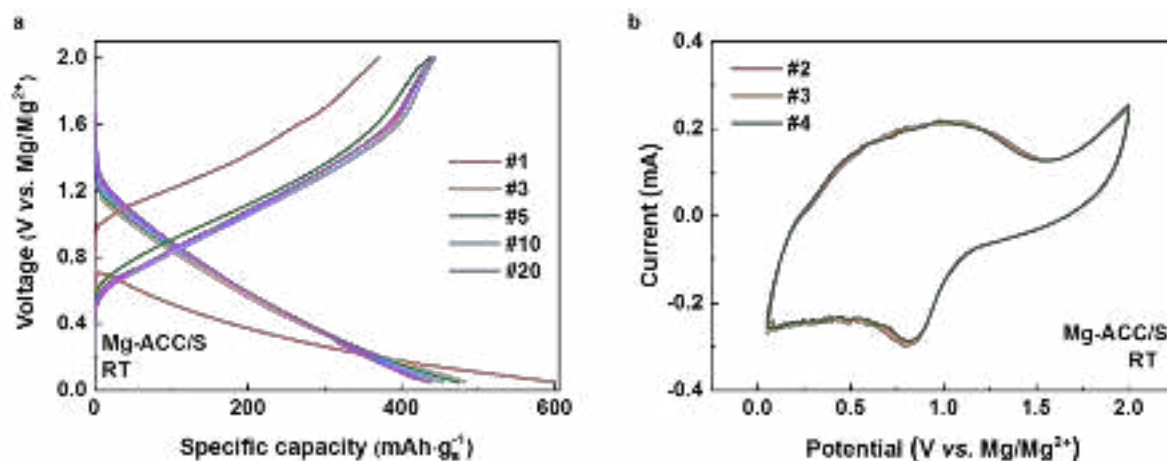
Figure S15. a) Voltage curves of the Mg||MLT-GPE||ACC/S cell charged/discharged at 0.2 C at room temperature; **b)** typical CV curves of the Mg||MLT-GPE||ACC/S cell, scan rate: 0.2 mV·s^{-1}; **c)** electrochemical performance of the Mg||liquid electrolyte||ACC/S cell.

After the initial cycle, the voltage curves of the Mg||MLT-GPE||ACC/S cell in Figure S15a shows sloped regions during discharging and charging starting from 1.2 V and 0.5 V respectively, which is in accordance with the typical CV curves in Figure S15b.
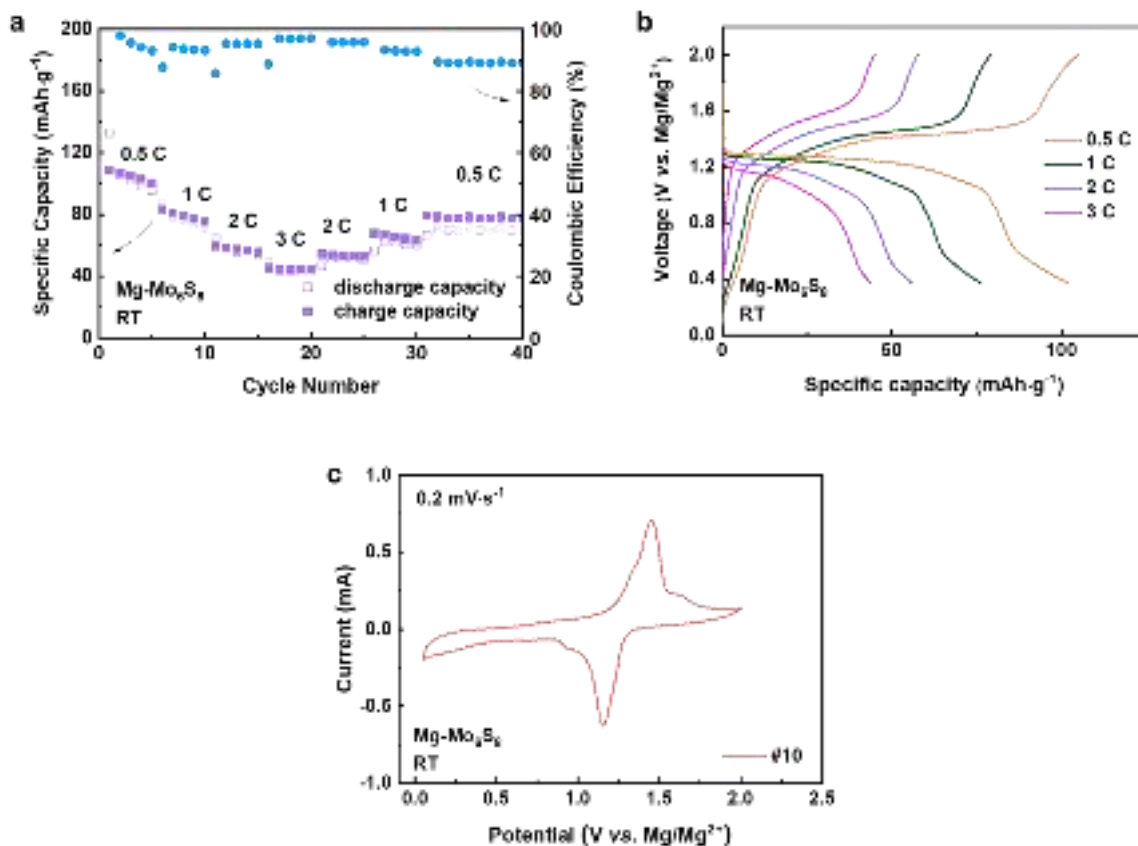
Figure S16. Mg||MLT-GPE||Mo₆S₈ cells: **a)** rate capability test (0.5 C, 1 C, 2 C, 3 C); **b)** voltage curves from S16a; **c)** CV curves at a scan rate of 0.2 mV·s⁻¹.

A Chevrel phase Mo_6S_8 cathode was tested together with a Mg foil and the MLT-GPE (Figure S16). The Mg||MLT-GPE|| Mo_6S_8 cell shows good rate capability when cycling the cell from 0.5 C to 3 C (Figure S16 a). A relatively high discharge capacity of ca. 80 mAh·g⁻¹ could be delivered at 0.5 C. The voltage curves and the CV shown in Figure S16b and c shows plateaus and featured redox peaks, indicating the successful cation insertion and extraction.
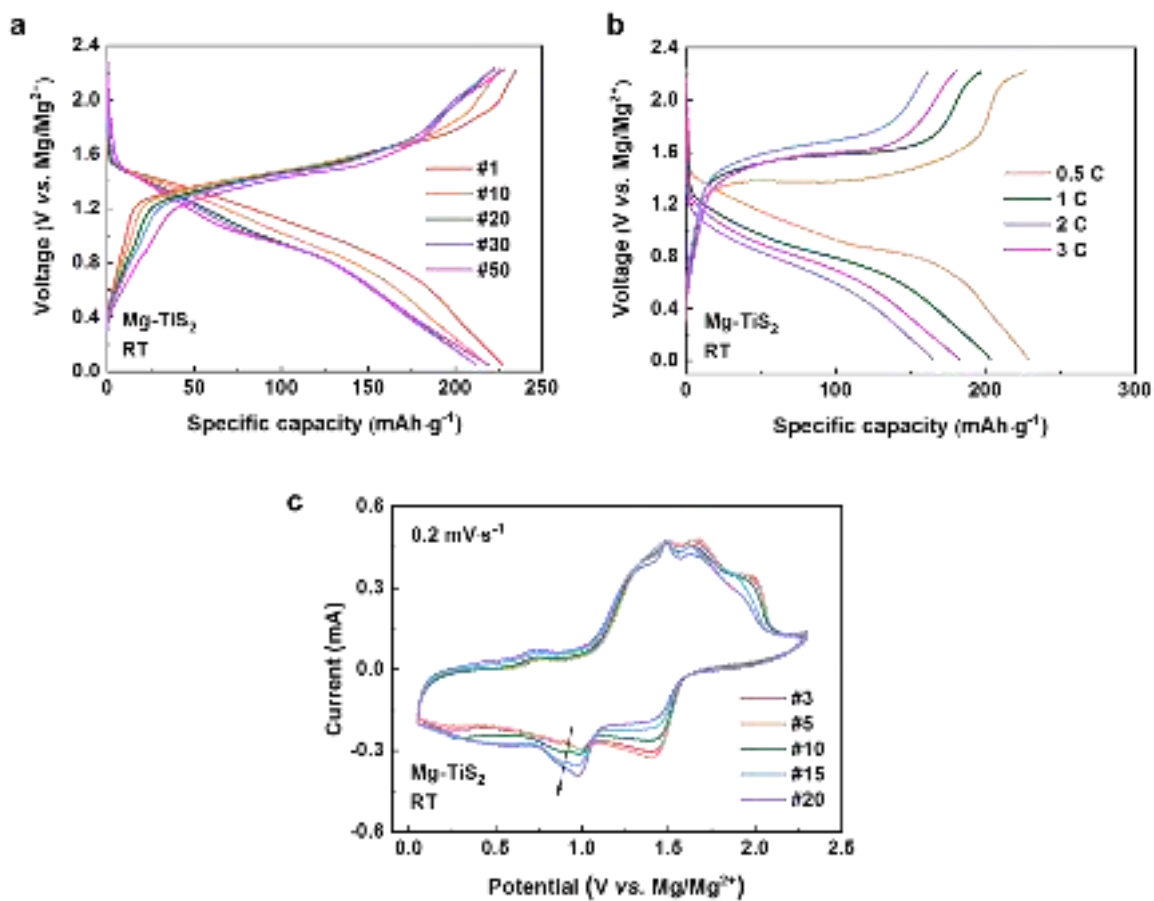
Figure S17. Mg||MLT-GPE||TiS$_2$ cells: **a)** voltage curves from Figure 5a; **b)** voltage curves from Figure 5b; **c)** CV curves at a scan rate of 0.2 mV·s^{-1}.
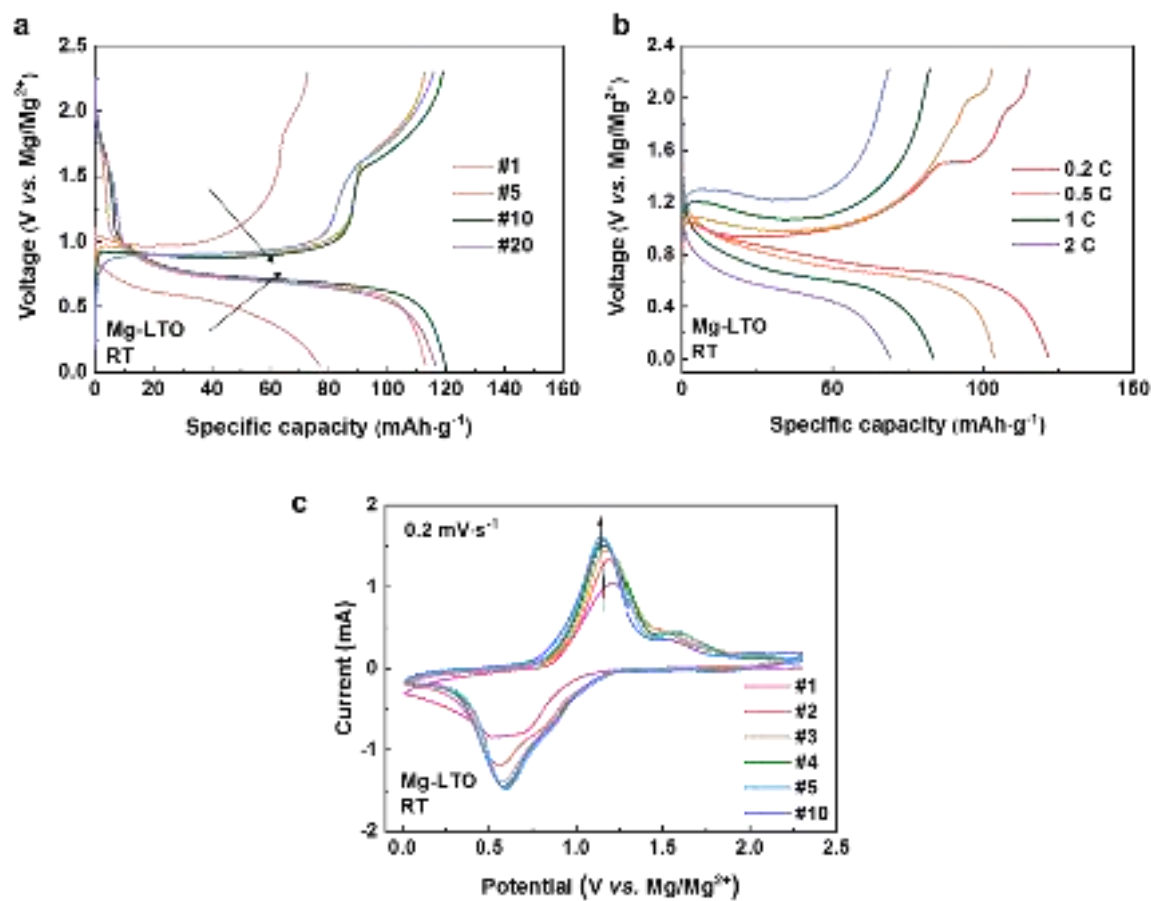
Figure S18. Mg||MLT-GPE||LTO cell: **a)** voltage curves from Figure 5c; **b)** voltage curves from Figure 5d; **c)** CV curves at a scan rate of 0.2 mV·s⁻¹.

Section 2. Supporting Tables

Table S1. Calculated resistance and ionic conductivity of MLT-GPE at different

temperatures from Figure 2a.

Temperature (° C)	R1 (Ω)	Ionic conductivity (S·cm^{-1})
0	105.7	1.46×10^{-4}
10	98.9	1.56×10^{-4}
20	89.9	1.72×10^{-4}
30	79.4	1.94×10^{-4}
40	69.3	2.23×10^{-4}

Table S2. Calculated resistance and ionic conductivity of the GPE without TiO$_2$

additive at different temperatures from Figure S4.

Temperature (° C)	R1 (Ω)	Ionic conductivity (S·cm^{-1})
0	263.7	5.87×10^{-5}
10	257.5	6.01×10^{-5}
20	227.2	6.81×10^{-5}
30	198.7	7.79×10^{-5}
40	173.1	8.94×10^{-5}

Table S3. Fitted resistance values before and after polarization .

	R1 (electrolyte resistance, Ω)	R2 + R3 (electrode resistance, Ω)
Before polarization	4352	8826/2 = 4413
Steady state	1223	20680/2 = 10340

Table S4. Comparison of the Mg-S cells performance with published work.

Cathode	Electrolyte	Current density	Cycle number	Capacity	Ref.
SPAN	MLT-GPE (solid)	0.2 C	140	580 mAh·g$_s^{-1}$	This
ACC/S		0.2 C	50	510 mAh·g$_s^{-1}$	work
CC@PANI+ MgS$_x$ catholyte	MACC (Liquid)	0.01 C	25	428 mAh·g$_s^{-1}$	[5]
S$_8$-MXene/carbon nanotube	Mg[B(hfip)$_4$]$_2$ (liquid)	0.03 C	25	400 mAh·g$_s^{-1}$	[6]
SPAN	MBA (liquid)	0.1 C	90	450 mAh·g$_s^{-1}$	[7]
VN/60S	MTB (liquid)	0.3 C	100	420 mAh·g$_s^{-1}$	[8]
S/NC	Mg[B(hfip)$_4$]$_2$+I$_2$ (liquid)	0.05 C	100	210 mAh·g$_s^{-1}$	[9]
S$_8$	THFPB (Liquid, 50°C)	0.06 C	25	915 mAh·g$_s^{-1}$	[10]
S/MC	MBA (liquid)	0.04 C	100	400 mAh·g$_s^{-1}$	[11]
S/MC	MTB (liquid)	0.05 C	55	390 mAh·g$_s^{-1}$	[12]
S/NC	Mg[B(hfip)$_4$]$_2$ (liquid)	0.02 C	50	200 mAh·g$_s^{-1}$	[13]
ACC/S	Mg[B(hfip)$_4$]$_2$ (liquid)	0.1 C	100	200 mAh·g$_s^{-1}$	[14]
S/rGO@PCC	Mg[HMDS]$_2$ (liquid)	0.01 C	40	400 mAh·g$_s^{-1}$	[15]

Table S5. Fitted resistance values from Figure S11.

Cycle number	R_1 (Ω)	R_2 (Ω)	R_3 (Ω)
5	20.59	35.53	4218
10	22.65	31.06	4673
15	25.02	34.84	5646
20	29.11	37.67	6698
25	32.67	34.12	6423
30	35.92	32.54	5743

Section 3. Supporting References

[1] A.B. Du, H.R. Zhang, Z.H. Zhang, J.W. Zhao, Z.L. Cui, Y.M. Zhao, S.M. Dong, L.L. Wang, X.H. Zhou, G.L. Cui, Adv. Mater., 31 (2019) 1805930.

[2] P. Wang, J. Trück, S. Niesen, J. Kappler, K. Küster, U. Starke, F. Ziegler, A. Hintennach, M.R. Buchmeiser, Batter. Supercaps, 3 (2020) 1239-1247.

[3] Z. Zhao-Karger, M.E.G. Bardaji, O. Fuhr, M. Fichtner, J. Mater. Chem. A, 5 (2017) 10815-10820.

[4] S. Waluś, C. Barchasz, R. Bouchet, F. Alloin, Electrochim. Acta, 359 (2020) 136944.

[5] D. Muthuraj, M. Pandey, M. Krishna, A. Ghosh, R. Sen, P. Johari, S. Mitra, J. Power Sources, 486 (2021) 229326.

[6] H. Kaland, F. Haskjold Fagerli, J. Hadler-Jacobsen, Z. Zhao-Karger, M. Fichtner, K. Wiik, N.P. Wagner, ChemSusChem, (2021).

[7] S. Zhang, Y. Huang, Y. NuLi, B. Wang, J. Yang, J. Wang, J. Phys. Chem. C, 124 (2020) 20712-20721.

[8] D. Huang, S. Tan, M. Li, D. Wang, C. Han, Q. An, L. Mai, ACS Appl. Mater. Interfaces, 12 (2020) 17474-17480.

[9] V. Bhaghavathi Parambath, Z. Zhao-Karger, T. Diemant, M. Jäckle, Z. Li, T. Scherer, A. Gross, R.J. Behm, M. Fichtner, J. Mater. Chem. A, (2020).

[10] Z. Zhou, B. Chen, T. Fang, Y. Li, Z. Zhou, Q. Wang, J. Zhang, Y. Zhao, Adv. Energy Mater, 10 (2019) 1902023.

[11] X. Zhao, Y. Yang, Y. NuLi, D. Li, Y. Wang, X. Xiang, Chem. Commun., 55 (2019) 6086-6089.

[12] Y. Yang, W. Wang, Y. Nuli, J. Yang, J. Wang, ACS Appl. Mater. Interfaces, 11 (2019) 9062-9072.

[13] B.P. Vinayan, H. Euchner, Z. Zhao-Karger, M.A. Cambaz, Z. Li, T. Diemant, R.J. Behm, A. Gross, M. Fichtner, J. Mater. Chem. A, 7 (2019) 25490-25502.

[14] Z. Zhao-Karger, R. Liu, W. Dai, Z. Li, T. Diemant, B.P. Vinayan, C. Bonatto Minella, X. Yu, A. Manthiram, R.J. Behm, M. Ruben, M. Fichtner, ACS Energy Lett., 3 (2018) 2005-2013.

[15] D. Muthuraj, A. Ghosh, A. Kumar, S. Mitra, ChemElectroChem, 6 (2018) 684-689.